J-based Magnetic Resonance Conductivity Tensor Imaging (MRCTI) at 3 T

M. Sadighi, C. Göksu, and M. Eyüboğlu, *IEEE Member*

***Abstract*— In this study, current density (J) - based Magnetic Resonance Conductivity Tensor Imaging (MRCTI) reconstruction algorithms namely, the Anisotropic Equipotential Projection (AEPP), the Anisotropic J-Substitution (AJS) and the Anisotropic Hybrid J-Substitution (AHJS) algorithms are implemented to reconstruct conductivity tensor images of a physical phantom using a 3T magnetic resonance imaging system. 10mA current pulses are injected in synchrony with a conventional spin-echo pulse sequence. Furthermore, a new J-based hybrid algorithm namely, the Anisotropic Hybrid Equipotential Projection (AHEPP) is proposed. In addition, reconstruction performances of the four algorithms are evaluated.**

Keywords- Magnetic resonance, imaging, conductivity tensor imaging, anisotropic conductivity imaging.

I. INTRODUCTION

Magnetic Resonance Electrical Impedance Tomography (MREIT) is a tomographic imaging technique, which provides cross-sectional conductivity images from measurements of magnetic flux densities due to externally injected currents [1]. But most of the biological tissues such as skeletal muscles, cardiac muscle and brain have anisotropic conductivities [2]. Hence, Magnetic Resonance Conductivity Tensor Imaging (MRCTI) is proposed to reconstruct the anisotropic conductivity distribution [3, 4].

Two types of anisotropic MRCTI reconstruction algorithms exist [3]. B-based algorithms use the magnetic flux density obtained from the MRI phase images to reconstruct images of conductivity tensors. J-based algorithms use the current density distribution, which is reconstructed from the measured magnetic flux density. In this study, J-based MRCTI algorithms are used to reconstruct anisotropic conductivity of an experimental phantom.

Several in vivo experimental MREIT studies have been performed on animals in recent years [5, 6, 7]. *In vivo* MREIT images of a human leg have also been obtained by using Harmonic B_z algorithm, which is a B-based isotropic MREIT reconstruction algorithm [8]. It is reported that the reconstructed conductivity images show quite different and unique contrast information in comparison to conventional MRI images. Similar studies are reported in [9] and [10]. Almost all of the MREIT reconstruction algorithms in literature assume isotropic conductivity distribution, which is actually may not be realistic for several biological tissues. In the case of anisotropy in a biological material, isotropic assumptions may result in erroneous conductivity reconstructions.

This project is partially funded by METU Research Grant BAP-07-02-2013-101 and Turkish Scientific and Technological Research Council (TUBITAK) Research Grant 113E301

M. Sadighi is with Dept. of Electrical and Electronics Engineering, Middle East Technical University (METU), 06800 Ankara/Turkey (e-mail: mehdi.sadighi@metu.edu.tr).

C. Göksu is with Dept. of Electrical and Electronics Engineering, METU, 06800 Ankara/Turkey (e-mail: cigoksu@metu.edu.tr).

M. Eyüboğlu. is with Dept. of Electrical and Electronics Engineering, METU, 06800 Ankara/Turkey (e-mail: meyub@metu.edu.tr).

II. MRCTI RECONSTRUCTION ALGORITHMS

A. Anisotropic Equipotential Projection (AEPP) Algorithm

In this algorithm, equipotential lines are constructed in the imaging region, using the measured current density distribution by projecting boundary potentials into the imaging region along equipotential lines. In the case of isotropic conductivity, the equipotential lines are perpendicular to the current density vectors but in the case of anisotropic conductivity the equipotential lines are only perpendicular to potential gradient ($\nabla\varphi$) lines. Therefore, by calculating the angle between the potential gradients and the current density vectors using (1), at any point (x, y) in the imaging region for known anisotropic conductivity values, the angle between equipotential lines and current density vectors can be calculated as,

$$\alpha_{\nabla\varphi|_{(x,y)}} = tan^{-1}\left(\frac{J_y\,\sigma_{xx} - J_x\,\sigma_{yx}}{J_x\,\sigma_{yy} - J_y\,\sigma_{xy}}\right)\Bigg|_{(x,y)\in S} \quad (1).$$

Boundary potential values are then projected into the imaging region using the measured current density distribution data and the angle $\alpha(x, y)$. α cannot be calculated at the first iteration since, the anisotropy is not known. Therefore, in calculation of initial conductivity distribution the current density vectors are assumed perpendicular to the equipotential lines.

B. Anisotropic J-Substitution (AJS) Algorithm

For an electrically conducting body Ω with resistivity ρ, the corresponding voltage V_ρ satisfies the boundary value problem (BVP) in (2),

$$\nabla.\left(\frac{1}{\rho}\nabla V_\rho\right) = 0 \qquad in\ \Omega$$
$$\frac{1}{\rho}\frac{\partial V_\rho}{\partial n} = J_I \qquad on\ \partial\Omega \quad (2).$$

On the other hand,

$$\boldsymbol{E_\rho}(r) := \left|\nabla V_\rho(r)\right| \tag{3}$$

where, $E_\rho(r)$ represents the internal electric field intensity [11, 12]. By solving the BVP in (2), a cost function can be considered as given in (3) to minimize the difference between the calculated current density distribution and the measured current density distribution reconstructed using MRCDI technique,

$$\Psi(\rho) := \int_\Omega \left|\boldsymbol{J}^*(r) - \frac{1}{\rho(r)}\,\boldsymbol{E_\rho}(r)\right|^2 \tag{4}.$$

In (4), $J^*(r)$ represents the magnitude of the internal measured current density. The updating strategy to minimize the residual sum in (4) is given in (5),

$$\bar{\bar{\sigma}}_m := \frac{\boldsymbol{J}^*(r_m)}{\boldsymbol{E_\rho}(r_m)} \tag{5}.$$

In (5), $\bar{\bar{\sigma}}_m$ is the newly calculated conductivity value for the body model element Ω_m, by using the $E_\rho(r_m)$ value, which was calculated at the center point of the Ω_m using the conductivity distribution in the previous iteration [11, 12].

C. Anisotropic Hybrid J-Substitution (AHJS) Algorithm

This algorithm is a combination of AEPP and AJS algorithms. First, the anisotropic conductivity is reconstructed by using AEPP and then the reconstructed conductivity is utilized in AJS algorithm as the initial conductivity distribution.

D. Anisotropic Hybrid Equipotential projection (AHEPP) Algorithm

This algorithm is also a combination of AEPP and AJS algorithms. The reconstructed anisotropic conductivity for one iteration of AJS algorithm is given to AEPP algorithm as the initial conductivity distribution and the algorithm starts iterating with this initial value.

III. Experimental Setup & Phantom

To evaluate the performance of the four algorithms experimentally, a phantom with four surface electrodes is designed. The designed phantom and its structure are shown in Fig. 1(a). Current steering structure shown in Fig. 1(b) is placed inside the phantom to mimic an anisotropic conductivity distribution in the phantom. The experimental phantom is filled with a saline solution of 0.2 S/m as the background of the phantom. To prepare the solution, 0.1 gr CuSO4 and 0.145 gr NaCl were mixed in 100 ml pure water.

A 3T MRI scanner with 70cm bore diameter and 45 mT/m gradient strength is used for data acquisition. The spin echo pulse sequence in [13], with the parameters given in Table I, is used in synchrony with a controllable current source injecting 10 mA current pulses into the imaging slice.

TABLE I. Experimental parameter values used during the data acquisition

Field of View (FOV)	***128mm***
Number of Frequency & Phase encoding	***64***
Number of Signal Averaging	***16***
Slice Thickness	***6mm***

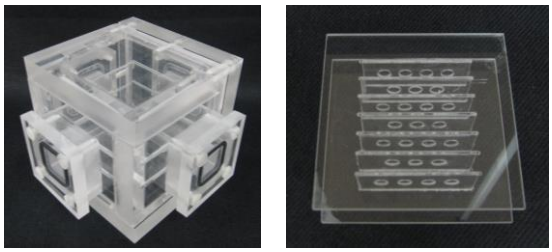

(a) (b)

Figure 1. (a) Experimental phantom (b) Current steering object

IV. Error Calculation

In order to evaluate the accuracy of the reconstructed conductivity images from the experimental data, an error formula is used as given in (6),

$$\varepsilon_{\sigma_n} = \sqrt{\frac{1}{N}\sum_{j=1}^{N}\frac{(\sigma_{jt_u} - \sigma_{jr_u})^2}{{\sigma_{jt_u}}^2}} \times 100\% \tag{6}.$$

In (6), σ_{jt_u} and σ_{jr_u} are the true and reconstructed conductivity values of the j^{th} pixel in anisotropic conductivity direction u (*xx, yy*), respectively and *N* is the total number of pixels in the conductivity image.

The true anisotropic conductivity of the experimental phantom is not known therefore, a 3D Finite Element (FE) model of the phantom is employed to estimate a true conductivity distribution of the phantom. Using the FE model, MRCTI forward problem is solved hence, the potential and the current density distributions are calculated for a known background conductivity distribution with specified boundary conditions, in the selected slice. By knowing the potential distribution in the selected slice it is possible to calculate the directional gradients of potential in *x* and *y* directions ($\nabla\varphi_x$, $\nabla\varphi_y$) for each pixel in the simulated imaging region. Estimated values of true anisotropic conductivity for each pixel can be calculated as given in (7) and shown Fig. 2.

$$\sigma_{xx} = -\frac{J_x}{\nabla\varphi_x}$$
$$\sigma_{yy} = -\frac{J_y}{\nabla\varphi_y} \tag{7}.$$

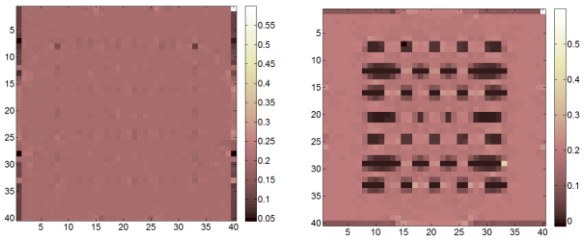

(a) (b)

Figure 2. Estimated true conductivity distributions calculated using the FE model using (7) (a) σ_{xx} (b) σ_{yy}

V. Experimental Results and Discussion

The reconstructed conductivity images (σ_{xx}, σ_{yy}), using AJS and AHEPP algorithms are presented in Fig. 3 and Fig. 4, respectively. As the reconstructed conductivity images using AEPP and AHJS algorithms are very erroneous to the extent that they cannot be evaluated using error measures [14], the related conductivity images are not given. Percentage errors of the reconstructed conductivities using AJS and AHEPP algorithms are given in Table II.

In *J*-based MRCTI reconstruction algorithms, the current density distribution inside the imaging region is reconstructed by Ampere's Law. The experimentally measured magnetic flux density is noisy. Taking the curl of this noisy data amplifies the noise in the reconstructed current density distribution. Using the noisy current density data in AEPP algorithm causes projection of the boundary potentials to the wrong pixels in the imaging region. Subsequently, a wrong potential gradient is calculated and the reconstructed anisotropic conductivity becomes highly erroneous. The reconstructed conductivities using the AHJS algorithm show similar results with the AEPP. In this algorithm the reconstructed conductivity images using AEPP algorithm is fed to AJS as initial conductivity distribution. But, starting the AJS algorithm with an extremely erroneous data causes highly erroneous conductivity image.

In the case of AJS algorithm, the potential field in the imaging region is calculated using FE method. Therefore, the calculated potential gradient in the imaging region is independent of the noisy current density data. However, the noisy current density data distorts the reconstructed conductivity images. Therefore, the reconstructed anisotropic conductivities in Fig. 3 are perceptually good, along with reduced calculated errors. The black regions at the corners of the reconstructed images shown in Fig. 3, are related to the pixels with negative conductivity values in σ_{yy} image and the very large positive values in the σ_{xx} image. As the negative conductivity value is not meaningful, zero conductivity is assigned to these pixels. Similarly, in the case of very large positive values at the corners of σ_{xx} image, pixels with values ten times greater than the conductivity of the background are set to zero conductivity. Furthermore, those regions are not included in the error calculation.

In AHEPP algorithm, unlike the AHJS algorithm, anisotropic conductivity distribution resulted from the first iteration of AJS is fed to AEPP algorithm as an initial conductivity distribution. This procedure can solve the problem of the AEPP algorithm in the case of isotropic assumptions in the first iteration. On the other hand, by starting the AEPP algorithm with an acceptable conductivity distribution with reduced error a better result is obtained. Furthermore, the entire time which is needed to obtain the desired conductivity distribution (Fig. 4), using this algorithm is about one tenth of the time, which is needed for the AJS algorithm to reach to the desired conductivity result for the same number of iterations (Fig. 3).

Constructing an exact true conductivity distribution for the experimental anisotropic conductivity phantom is not possible. Therefore, the calculated error values do not reflect the exact ability of the algorithms in reconstructing conductivity tensor. The error calculation formula in this study is used to attribute a numerical value to the accuracy of the reconstructed images, also to compare the algorithms with each other.

As the final comparison of the four *J*-based MRCTI reconstruction algorithms, the increased error at the corners of the reconstructed conductivity images is discussed. The current density data at the corner regions of the experimental phantom is the minimum. Therefore, current density data at these points is more sensitive to the experimental noise and these regions in the reconstructed conductivity images of all of the four algorithms are more erroneous.

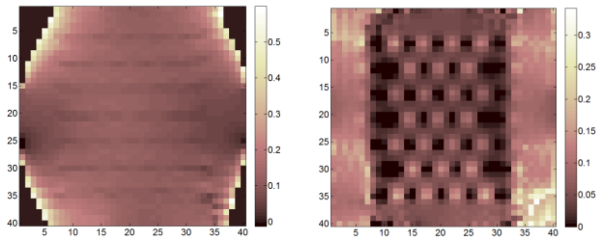

(a) (b)

Figure 3. The images of anisotropic conductivity reconstructed using AJS algorithm for the experimental phantom (a) σ_{xx} (b) σ_{yy}. Scales are in S/m.

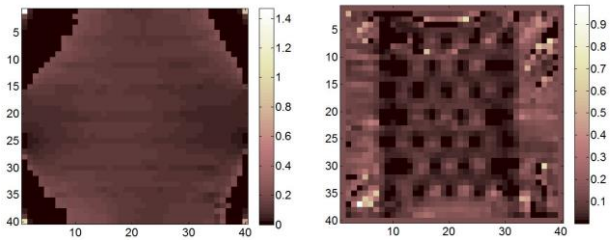

(a) (b)

Figure 4. The images of anisotropic conductivity reconstructed using AHEPP algorithm for the experimental phantom (a) σ_{xx} (b) σ_{yy}. Scales are in S/m.

TABLE II. Percentage error of the reconstructed conductivities using AJS and AHEPP algorithms

Anisotropic Conductivity	σ_{xx}	σ_{yy}
Error percentage for AJS	40.04	53.66
Error percentage for AHEPP	61.56	58.98

But, it can be inferred from Fig. 3-4, that this increased error at the corners of the reconstructed conductivity images using AJS is the minimum where in the case of AEPP algorithm is the maximum. Because, the AEPP algorithm is more sensitive to the current density noise whereas the AJS has the least sensitivity to current density noise in conductivity calculation. The effect of this error sensitivity is better visible in the resultant conductivity images from the AHEPP algorithm in comparison to the AJS in the *yy* direction (σ_{yy}), because a main body of the AHEPP algorithm is based on the AEPP algorithm.

VI. Conclusion

The reconstruction performances of the four J-based MRCTI reconstruction algorithms are compared and illustrated using the performance chart of Fig. 5 [14]. The information about the reconstruction quality by using simulated measurements and the corresponding errors in the chart are taken from [15].

As it can be inferred from the chart, when measured data is used, the J-Substitution algorithm has the best reconstruction performance. Furthermore, by considering all aspects of simulation and experimental applications, the proposed AHEPP algorithm shows a good overall performance. This algorithm inherits the good performance of the AEPP algorithm in reconstructions using simulated measurements along with low time consumption and low memory usage, because the main body of this algorithm is the AEPP algorithm. Similarly, the good performance of the AJS algorithm in experimental applications can be seen in AHEPP algorithm as well. The best performance in the simulation applications belongs to AHEPP algorithm where, in the experimental applications AJS algorithm shows the best results and AHEPP is in the second place. The conductivity images reconstructed in this study, in comparison to the results obtained in [13], using 0.15T METU-EEE MRI system and injecting 20mA current pulses, show perceptual improvement due to better signal to noise ratio (SNR) and spatial resolution. This improvement is more visible in the results of AJS algorithm. In both studies,

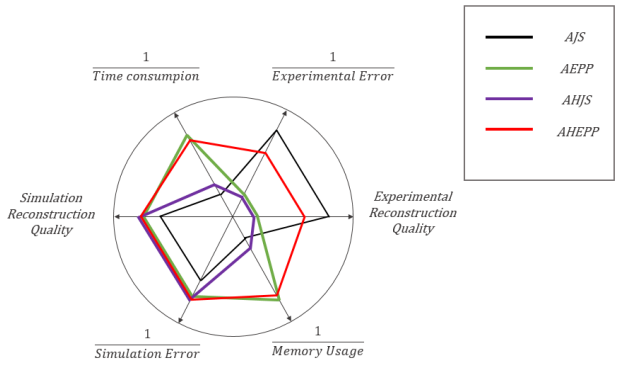

Figure 5. The performance chart of the four *J*-based reconstruction algorithms in reconstructing both simulated and experimental measurements. In the chart, the algorithms with wider area have better performance.

AJS algorithm shows the best performance in reconstruction of experimental data among the J-based MRCTI algorithms. In addition, due to better SNR of the 3T MRI scanner in comparison to the 0.15T METU-EEE MRI system, total data acquisition time is reduced by reducing the number of signal averaging. Furthermore, the amplitude of the injected currents into the imaging slice in this study is one half of the value applied in [13], which is more desirable and promising to be reduced even more for application of the technique to *in vivo* imaging.

References

[1] B. M. Eyüboğlu, "Magnetic Resonance - Electrical Impedance Tomography," WILEY - Encyclopedia of Biomedical Engineering, In WILE Y-Encyclopedia of Biomedical Engineering (Metin Akay, ed.), vol.4, pp. 2154-2162, 2006.

[2] L. A. Geddes and L. E. Baker, "The specific resistance of biological material—a compendium of data for the biomedical engineer and physiologist," *Med. Biol. Eng.* vol. 5, no. 3, pp. 271–293, May. 1967.

[3] E. Değirmenci and B. M. Eyüboğlu, "Image reconstruction in magnetic resonance conductivity tensor imaging (MRCTI).," *IEEE Trans. Med. Imaging*, vol. 31, no. 3, pp. 525–32, March. 2012.

[4] E. Değirmenci, B. M. Eyüboğlu, "Anisotropic Conductivity Imaging with MREIT Using J-substitution and Hybrid J-substitution Algorithms," in *Proc. World Congress on Medical Physics and Biomedical Engineering,* Munich, Germany, 2009, pp. 308-311.

[5] K. Jeon, A. S. Minhas, Y. T. Kim, W. C. Jeong, H. J. Kim, B. T. Kang, H. M. Park, C.-O. Lee, J. K. Seo, and E. J. Woo, "MREIT conductivity imaging of the postmortem canine abdomen using CoReHA.," *Physiol. Meas.*, vol. 30, no. 9, pp. 957–66, Sep. 2009.

[6] H. J. Kim, W. C. Jeong, Y. T. Kim, a S. Minhas, T. H. Lee, C. Y. Lim, H. M. Park, J. K. Seo, and E. J. Woo, "In vivo conductivity imaging of canine male pelvis using a 3T MREIT system," *J. Phys. Conf. Ser.*, vol. 224, p. 012020, Apr. 2010.

[7] Y. T. Kim, Z. Meng, A. S. Minhas, H. J. Kim, E. J. Woo, C. Y. Lim, and H. M. Park, "In vivo MREIT conductivity imaging of canine brain to evaluate ischemia and abscess," *2011 8th Int. Symp. Noninvasive Funct. Source Imaging Brain Hear. 2011 8th Int. Conf. Bioelectromagn.*, pp. 44–47, May 2011.

[8] H. J. Kim, Y. T. Kim, A. S. Minhas, W. C. Jeong, E. J. Woo, J. K. Seo, and O. J. Kwon, "In vivo high-resolution conductivity imaging of the human leg using MREIT: the first human experiment.," *IEEE Trans. Med. Imaging*, vol. 28, no. 11, pp. 1681–7, Nov. 2009.

[9] Y. T. Kim, A. S. Minhas, Z. Meng, H. J. Kim, and E. J. Woo, "Conductivity imaging of human lower extremity using MREIT with multi-echo pulse sequence and 3 mA imaging current," *2011 8th Int. Symp. Noninvasive Funct. Source Imaging Brain Hear. 2011 8th Int. Conf. Bioelectromagn., pp. 48–52, May 2011.*

[10] E. J. Woo, "High-resolution MREIT using low imaging currents.," *Conf. Proc. IEEE Eng. Med. Biol. Soc.,* vol. 2011, pp. 7025–8, Jan. 2011.

[11] O. Kwon, E. J. Woo, J. Yoon, and J. K. Seo, "Magnetic Resonance Electrical Impedance Tomography (MREIT): Simulation Study of J-Substitution Algorithm," *IEEE Trans. Biomedical Engineering*, vol. 49, no. 2, pp. 160–167, 2002.

[12] H.S. Khang, B. Il Lee, S. H. Oh, E. J. Woo, S. Y. Lee, M. H. Cho, O. Kwon, J. R. Yoon, and J. K. Seo, "J-substitution algorithm in magnetic resonance electrical impedance tomography (MREIT): phantom experiments for static resistivity images.," *IEEE Trans. Med. Imaging*, vol. 21, no. 6, pp. 695–702, Jun. 2002.

[13] E. Değirmenci and B. M. Eyüboğlu, "Practical realization of magnetic resonance conductivity tensor imaging (MRCTI).," *IEEE Trans. Med. Imaging*, vol. 32, no. 3, pp. 601–608, March. 2013.

[14] M. Sadighi, "Magnetic Resonance Conductivity Tensor Imaging (MRCTI) At 3 Tesla," M.S. thesis, Dept. Elect. Eng., METU Univ., Ankara, Turkey, 2014.

[15] E. Değirmenci, "High resolution imaging of anisotropic conductivity with magnetic resonance electrical impedance tomography (MREIT)," Ph.D. dissertation, Dept. Elect. Eng., METU Univ., Ankara, Turkey, 2010.